Unraveling hole interlayer-dependent interfacial energetics of LEDs

Cheng Yan, Xiankan Zeng, Qungui Wang, Xiaodong Peng, Wen Li, Jingjing Cao, Yue Gao, Xiang Chu, Xuehai Fu, Shiyu Yang, Yongjian Chen, Weiqing Yang *

Key Laboratory of Advanced Technologies of Materials (Ministry of Education), School of Materials Science and Engineering, Southwest Jiaotong University, Chengdu 610031, PR China

ARTICLE INFO

ABSTRACT

To fundamentally understand the underlying interfacial physics of hole transporting layer is a key to rotationally engineer high-performance light-emitting diodes (LEDs). Here, we unravel the hole interlayer-dependent interfacial energetics of LEDs via combining imaged contact potential/polarization difference, and multi-time scale capacitance/voltage response. A universally existing but undesired stagnation of current density with voltages, under the direct contact of light-emitting Poly-TPD with electrodes, was proved to be rooted from the alternant dominance of capacitance/resistance behaviors with alternating strong/weak polarizations of Poly-TPD. The introduction of hole interlayer (PEDOT:PSS) with more disordered polarization direction and greater intensity can build plentiful carrier hopping channels and ensure the rapidly dynamic charge transfer from electrodes to Poly-TPD, conducing to the increased capacitive reactance contribution at low voltages and inductive effects at high voltages. Also, we clarify its frequency-response difference for emerging high-speed modulation application. This discovery might enable us to explore the next-generation high-efficiency display and optical data-communication.

1. Introduction

The fundamental understanding and exploiting of underlying interfacial physics is key in rotationally engineering breakthroughs for light emitting diodes (LEDs), a system-level collaborative device with multi-functional components. Hole transporting layers (HTLs), mainly implementing hole injection and transport, are essential for high-performance LEDs [1–3]. Unfortunately, typical electrodes used in LEDs, such as indium-tin oxide (ITO), give rise to large injection barriers when contacting organic HTLs with high ionization energy [4].

The buffer layers have been successfully employed to achieve the unimpededly charge transfer between injector and emitter. Among them, poly(3,4-ethylenedioxythiophene) polystyrene sulfonate (PEDOT:PSS) and poly(N,N′-bis-4-butylphenyl-N,N′-bisphenyl)benzidine (Poly-TPD) are two outstanding candidates. Significantly, PEDOT:PSS for hole transporting features more semi-metallic characteristics [5], whereas Poly-TPD could be used as a blue emitter in addition to being able to transport holes [6]. It had been verified that meager electronic interface between injector and emitter could be successfully meliorated by adopting multi-HTLs, featuring stepped and gradient electronic profiles [3,7]. Therefore, bilayer architecture of PEDOT:PSS/Poly-TPD is

adopted [8,9]. And sometimes, they appear solely, the only HTL between electrodes and emitters [7,10–12]. Nevertheless, a universally observable stagnation of current density with increasing voltages appears in LEDs with ITO/Poly-TPD/Emitter structure, unfortunately, it has been habitually ignored [11,13–15]. Until the end of this worthless stagnation and the start of the second growth, the electroluminescence (EL) will not occur, which undoubtedly increases the energy consumption. More seriously, the heterogeneous characteristics of interfacial charges arising therefrom will significantly affect the strength and distribution of local electric field, engendering irremediable calamity to electrical performance of LEDs in terms of breakdown and operational reliability [16,17]. This calls for a deeper interfacial investigation, rather than simply adapting HTLs according to the gradient energy level criterion. For avoiding the trial-and-error circle, it is vital to dissect HTL-dependent interfacial information and unravel relative physics phenomenon, and meanwhile, to establish sieving principle for validity range of appropriate charge-transporting parameters.

In this regard, we elucidate the hole interlayer-dependent carrier dynamics and energetics of LEDs by combining kelvin probe force microscopy (KPFM) featuring imaged contact potential/polarization difference, and impedance spectroscopy featuring multi-time scale

capacitance/voltage response. Resultantly, we find that Poly-TPD possesses regular namatic stripes with alternating strong/weak polarizations. This ordered alternating polarization distribution is the main cause of the alternant dominance of capacitance/resistance behaviors with increasing voltages when Poly-TPD directly contacts ITO electrode. Such alternating capacitance/resistance behaviors will naturally result in a stagnation of current density for LEDs, only at the end of this situation can efficient electroluminescence (EL) be produced. The mounting of hole interlayer (PEDOT:PSS) with the disordered polarization reduces electrode polarization and builds plentiful carrier hopping channels, ensuring the rapid and dynamic charge transfer between ITO and Poly-TPD. This conduces to the prominent capacitive reactance behaviors at low voltages and increased inductive effects, enabling current density-voltage of LEDs a standard diode exponential change. Besides, we clarify its frequency-response difference for emerging optical data-communication application. This work provides a fresh insight to unravel interfacial physics of LEDs toward next-generation high-efficiency display and high-speed optical data-communication.

2. Results and discussion

The typical ITO/HTL/Emitter/TPBi/LiF/Al structured LEDs with/without the hole interlayer (PEDOT:PSS) were designed (Fig. S1 and Experimental section). When the hole interlayer is absent, the current density-voltage (J-V) curve of perovskite LEDs (PeLEDs), exhibits a stagnation and two significant jumps (Fig. 1a-i). It is worth noting that the brightness from the electroluminescence (EL) process only starts to increase at the second jump (at 5.0 V), which means that carriers are injected into perovskite layer for exciton recombination and light emission, as shown in Fig. 1b-i and Fig. S2a. While after introducing hole interlayer, only one jump in the current density is observed, and the J-V exhibits a standard diode exponential change (Fig. 1a-ii). Even at the driving voltages lower than 3 V, the EL at a peak wavelength of 513 nm could also be detected (Fig. 1b-ii, Fig. S2b). Hole interlayer-dependent organic LEDs (OLEDs) further verified the similar change law of J-V during carrier injecting process. Fig. 1c-i demonstrates a secondary increase in current density, and a larger turn-on voltage (6 V) of interlayer-

free OLEDs (Fig. S2c). As predicted, unimpededly interfacial hole transport enables one jump in current density curve and a smaller turn-on voltage (2.5–3.0 V) of OLEDs with hole interlayer (Fig. 1c-ii). The broadening and splitting of EL peak (at 429 nm) are attributed to the distribution difference of carriers at light-emitting interface, also the coexistence of monomer and excimer emissions in Poly-TPD films (Fig. S2d) [18,19]. Circumstanced by the direct contact between electrodes and Poly-TPD, the first jump of current density is smooth at 3 V, which almost equals to the bandgap (E_g) of Poly-TPD divided by the elementary charge (q). The holes actually used for EL do not work until the first jump stabilizes, and current efficiency can only be manifested at higher voltages (Fig. S3). And the greatly improved electron-photon conversion efficiency can be achieved at lower voltages aided by interlayer. During the operation of LEDs, the injection of excess charge will not only reduce the conversion ratio of electron-to-photon and consume electrical energy, but also aggravate the premature aging of functional layers [20,21]. Unfortunately, this phenomenon of worthless stagnation in current density has not attracted enough attention. Hole interlayer-dependent interfacial landscape calls for in-depth dissection.

Since the simultaneous existence of carrier injection and exciton emission will greatly increase the analysis complexity, it is necessary to decouple LEDs and penetratingly explore injected energetics of hole-only devices. In such a device, the sandwiched hole injector between two electrodes prevents the injection of electron and ensures the exclusively carried current by holes when applying the voltage [4]. Here, hole-only devices feature an architecture of ITO/HTL/MoO₃/Al. Among them, HTL represents PEDOT:PSS, Poly-TPD, PEDOT:PSS/Poly-TPD, respectively. Fig. 2a exhibits sequentially descending current density in PEDOT:PSS, Poly-TPD and bilayer hole-only devices, whether it is forward or reverse voltage scanning. The differences are expected as PEDOT:PSS ($\sim 10^{-2}$ cm² V^{-1} s^{-1}) owns several orders of hole mobility greater than Poly-TPD ($\sim 10^{-4}$ cm² V^{-1} s^{-1}) and lower interfacial barrier when contacted with ITO [22]. Ascribing to the lower hole-injection barrier existing at Poly-TPD/MoO₃ interface, the current injected from MoO₃ is a little higher than that from ITO, for Poly-TPD and bilayer HTL devices. D-value of current density (ΔJ) between forward (positive) and reverse (negative) voltage scanning further reveals this trend (Fig. 2b).
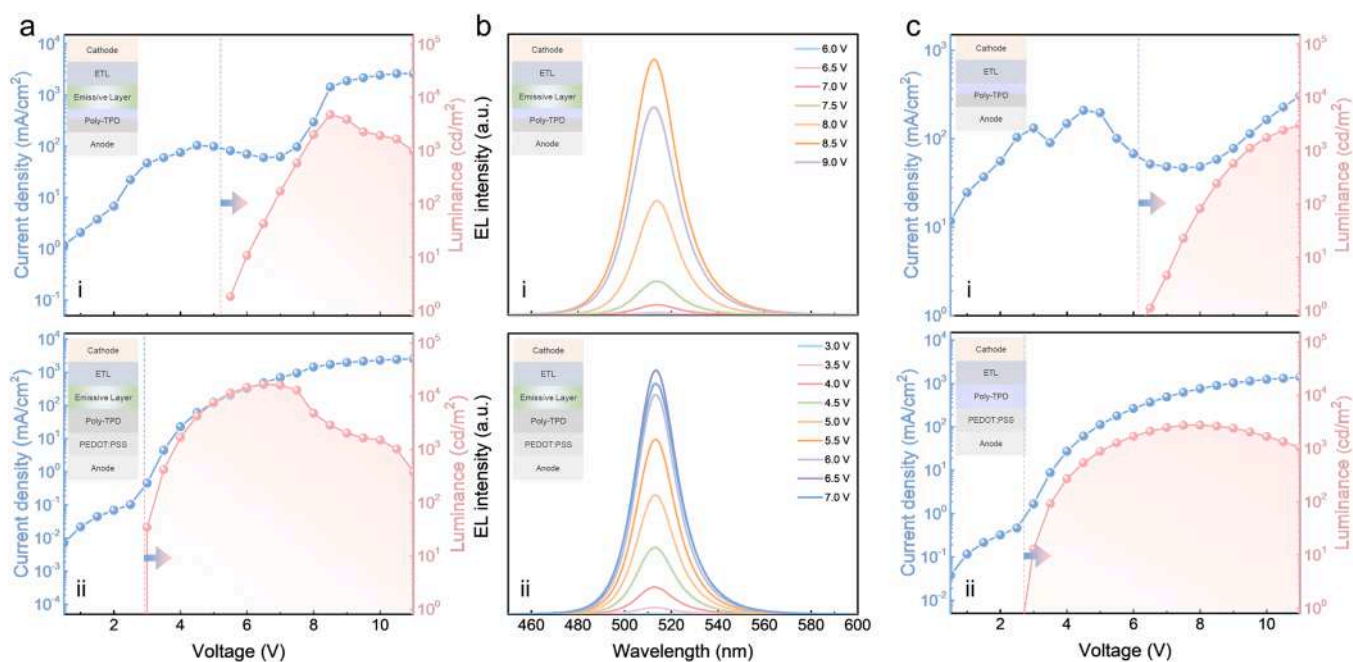
Fig. 1. Schematic diagram and device performance of hole interlayer-dependent LEDs. (a) Current density and luminance of perovskite LEDs (i) without and (ii) with PEDOT:PSS. (b) EL spectra of perovskite LEDs (i) without and (ii) with PEDOT:PSS. (c) Current density and luminance of organic LEDs (i) without and (ii) with PEDOT:PSS.
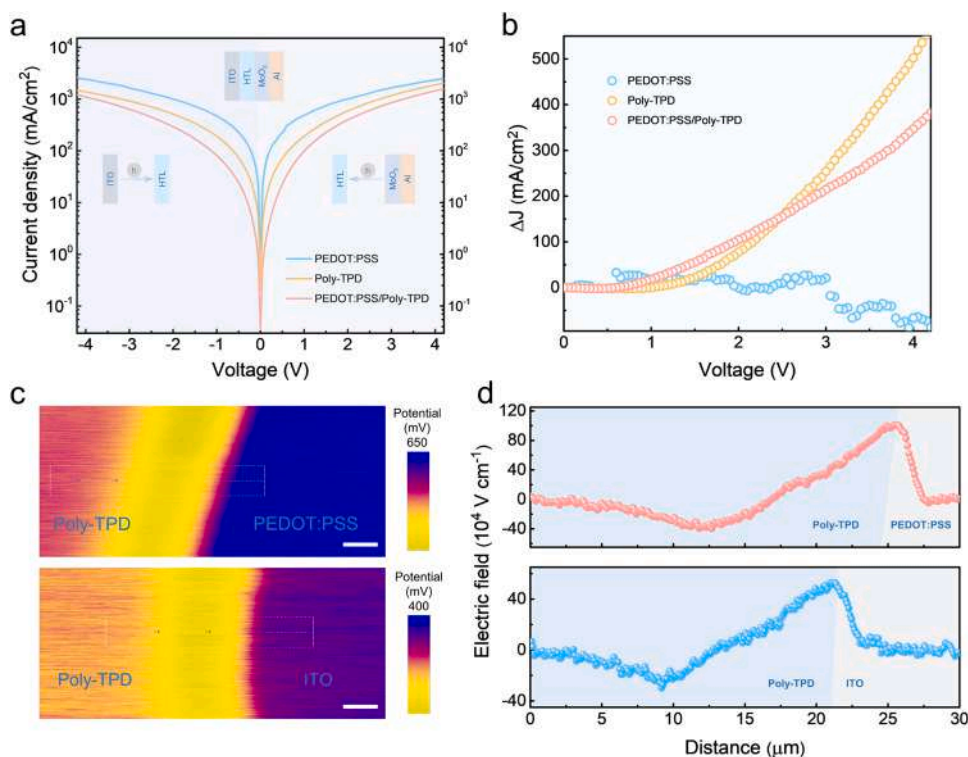
Fig. 2. Hole interlayer-dependent contact energetics. (a) Current density–voltage characteristics and (b) current density difference between positive bias and negative bias sweep of ITO/Poly-TPD/MoO$_3$/Al and ITO/PEDOT:PSS/Poly-TPD/MoO$_3$/Al hole-only device. Negative bias corresponds to hole injection from the ITO, positive bias to hole injection from MoO$_3$. (c) Surface potential images from KPFM Characterizations. (d) The corresponding electric field distribution of PEDOT:PSS and ITO surface partially covered with Poly-TPD, respectively. The scale bar is 5 μm.

The increasing ΔJ of Poly-TPD with voltages suggests the current amplification caused by interfacial barrier of electrode/Poly-TPD. Dissimilarly, ΔJ value of PEDOT:PSS device oscillates within a relatively fixed interval substantially greater than zero during low-voltage scanning. When the voltage rises to 3 V, the jump of the injected current from ITO side makes ΔJ show a descending trend. This may be attributed to the diffusion of high kinetic energy MoO$_3$ clusters into the adjoining PEDOT:PSS upon thermal evaporation to construct a locally efficient p-doped interface [23], which comes into play at high electric fields to facilitate carrier transfer and increase current injected from ITO (Fig. S4). This implies that the difference in spatiality and energetics of two amorphous semiconductors result in distinctly injected landscape when they contact with electrodes. PEDOT:PSS is mainly endowed with half-metallic characteristics of delocalized states and less affected by injection limitation, while Poly-TPD possesses localized states and is more sensitive with barriers. As for bilayer device, the earlier onset and slower growth rate of ΔJ with increasing voltages occur, which certifies that current density amplification could be significantly alleviated after the insertion of PEDOT:PSS. Upon logarithmic conversion of positive voltage scanning, the space charge effects of three devices are shown in Fig. S5 (also in Supporting Note 1). The injection-limited ohmic regime of PEDOT:PSS is wider than that of Poly-TPD, implying that Poly-TPD is more susceptible to space charge effects than PEDOT:PSS. In contrast, bilayer device reaches SCL region even at lower applied voltages (0.2 V), which is 0.6 V lower than that of the Poly-TPD device (0.8 V) to reach SCL, further proving the alleviating effect of hole interlayers on interface barriers.

J-V characteristics preliminarily evaluate injection energetics in hole-only devices, but the hypothesized mechanism of interfacial contact requires extra cross-certification. Kelvin probe force microscopy (KPFM) is widely used a functional imaging technique to analyze interfacial band alignment by measuring the contact potential difference (CPD) between samples and tips. Considering that the key of hole interlayer-dependent devices lies in different substances in contact with Poly-TPD and ITO, KPFM visualizes the interfacial CPD of Poly-TPD/PEDOT:PSS and Poly-TPD/ITO. Fig. 2c depicts the visualized images

of uniform surface potential (SP) in both Poly-TPD and adjacent substance area below. Owing to marginal accumulation of spin-coated materials, an abrupt bump of topography appears at the transitional region, the darker color, the higher SP (Fig. S6a, b). And more visible color difference indicates the larger CPD at Poly-TPD/PEDOT:PSS interface when compared with Poly-TPD/ITO interface. For a finer exhibition of this change, the line profiles were extracted. The Poly-TPD film with a thickness of 70 nm above PEDOT:PSS induces negative 240 mV CPD (Fig. S6c). Nevertheless, when contacting with ITO, the Poly-TPD film with a thickness of 57 nm induces a 130 mV CPD (Fig. S6d). By taking derivative of extracted CPD profiles, the locally interfacial electric field was obtained (Fig. 2d). Interestingly, it is perceptible that electric field in PEDOT:PSS/Poly-TPD interface is stronger than that in ITO/Poly-TPD interface. The CPD (6 mV) between ITO and PEDOT:PSS is almost negligible compared to that of Poly-TPD/ITO and Poly-TPD/PEDOT:PSS interfaces (Fig. S7), thus the electric field intensity is also extremely weak. The band bending of Poly-TPD near PEDOT:PSS was enlarged [24]. And the interfacial dipoles induced by the hole interlayer promotes the charge transfer [25]. However, interfacial dipole-dependent carrier landscape still requires further investigation.

Interfacial polarization could occur at the heterogeneous interface, induced by the dipoles from hole interlayers. Profiting from the hysteresis measurement of drive signal and feedback signal by the amplitude channel in KPFM, the magnitude difference in polarization between PEDOT:PSS and Poly-TPD was directly observed. Regular nematic stripes occur on Poly-TPD films, while they are almost absent on the PEDOT:PSS films (Fig. 3a). Meanwhile, the more regular and ordered building block pattern in Poly-TPD than that in PEDOT:PSS further cross-checks the considerable difference in polarization direction between the two organic semiconductors, as the surface phase image shown in Fig. 3b. Under the same-area amplitude map (Fig. S8), the extracted percentage demonstrates that PEDOT:PSS has an average amplitude of 20 mV, greater than that of Poly-TPD (12 mV) (Fig. 3c), indicating enhanced interfacial polarization by semi-metallic semi-conducting interlayers. By drawing a line with the same length and
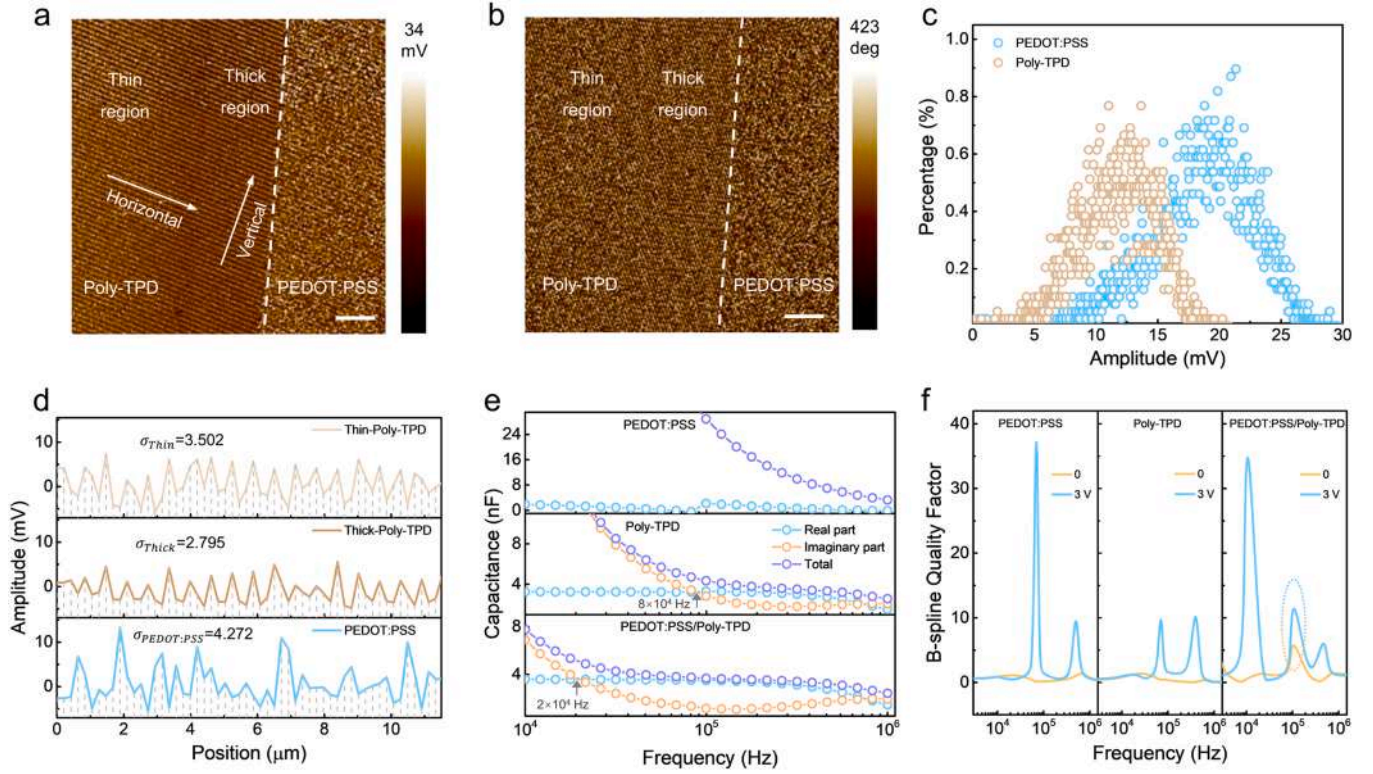
Fig. 3. Interfacial polarization and charge relaxation. (a) Surface amplitude and (b) surface phase images of Poly-TPD (left) partially spin-coated on PEDOT:PSS (right). Thin and thick indicate the thickness of Poly-TPD. The scale bar is 5 μm. The white arrow represents vertical or horizontal to the nematic stripes. (c) Extracted amplitude percentage of Poly-TPD and PEDOT:PSS. (d) The amplitude distribution extracted from the thin-Poly-TPD, thick-Poly-TPD and PEDOT:PSS regions when a line perpendicular to the nematic fringe passes, respectively. σ represents the standard deviation of amplitude values. (e) Real part (C′) and imaginary capacitance (C′ʹ), for hole-only devices, which is performed at 0 V steady-state voltage. (f) Frequency-dependent quality factor as a function of bias voltage for hole-only devices.

angle perpendicular to nematic stripes, the amplitude distribution passing from thin-Poly-TPD, thick-Poly-TPD and PEDOT:PSS regions was plotted in Fig. 3d. The thick Poly-TPD region presents the smallest standard deviation (σ), meaning the smallest relative dispersion of amplitude value. As a comparison, PEDOT:PSS region has the biggest σ. Considering that capacitive and resistive elements are directly related to charge injection, transport, accumulation in semiconductor devices [26], impedance spectroscopy featuring time-scale electrical response was used to investigate charge transport kinetics and relaxation process in hole interlayer-dependent single carrier devices. By applying a low-amplitude AC voltage of 30 mV to zero steady-state-potential devices, dynamical behaviors of electrode/HTL interface was better unraveled [27,28]. Nyquist plot indicates a distinct charge transport regime in Poly-TPD included devices, which is basically featured by one semicircle (Fig. S9a, inset is an enlarged view in high-frequency range). These semicircles near the origin accompanied with higher frequency spectrum attributes to charge transport-induced impedance [29,30]. The difference lies in that the bilayer system exhibits the wider radius. Although being characterized with negligible resistance in PEDOT:PSS-only device, when compared with the sole Poly-TPD system, its introduction fourfold increases the impedance of bilayer device. This also corroborates the current drop caused by the hole interlayer which increases overall resistance of devices. At the single Poly-TPD system, serious impedance oscillation happens in the low frequency regime (Fig. S9b). Nevertheless, the bilayer system not only transits smoothly, but also derives a second semicircle (Fig. S9c), probably arising from the charge transfer at PEDOT:PSS/Poly-TPD interface. Considering the device as a whole:

$$Z(\omega) = Z^{'}(\omega) + jZ^{'}\prime(\omega) \tag{1}$$

$$C(\omega) = \frac{1}{j\omega \times Z(\omega)} = C^{'}(\omega) - jC^{'}\prime(\omega) \tag{2}$$

where ω is the angular frequency (ω = 2πf), Z′ and Z′ʹ are the real and imaginary part of the impedance Z(ω), C′(ω) and C′ʹ(ω) are the real and imaginary part of the capacitance C(ω), respectively [31]. As plotted in Fig. 3e, when the real and imaginary part capacitance are equal, the frequency (f_0) separately locates at $\sim 2 \times 10^4$ Hz and $\sim 8 \times 10^4$ Hz in systems with and without hole interlayer, respectively. This frequency defines a relaxation time constant τ_0 ($\tau_0 = 1/f_0$), which represents a transition between capacitive behavior lower than f_0 and resistive behavior higher than f_0. The time constant τ_0 increases from 12 to 50 μs when the interlayer is sandwiched between ITO and Poly-TPD. However, PEDOT:PSS-only devices cannot reach the appearing condition of relaxation time, meaning the dominant capacitive characteristics proportion and almost negligible resistive influence in disturbance frequency range. Under the lowest frequency (0.1 Hz), the responding capacitance of PEDOT:PSS device (0.027 F, Fig. S10a) is an order of magnitude lower than that of Poly-TPD (2.4×10^{-3} F, Fig. S10b), And bilayer devices demonstrate minimum capacitance of 6.4×10^{-4} F (Fig. S10c). This is consistent with the trend that the smaller time constant corresponds more obvious capacitive behaviors and higher electrode polarization [32]. Attributed to the distinctive monomer structure with additional side chains, the electron coupling was strengthened along the π-π stacking direction of Poly-TPD, by promoting the alignment of backbones in the 2D plane [33]. Nevertheless, PEDOT chain lacks side chains for promoting backbone rigidity of PEDOT:PSS, for this reason more chain vibration would appear as hopping channels [34]. Thereby, the hopping probability of charge transport in Poly-TPD is lower than that in PEDOT:PSS and negative capacitance behavior occurs at higher frequencies, as demonstrated in Fig. S11a. The negative

capacitance contribution of PEDOT:PSS (271 nF), shifts to a less variation in Poly-TPD (195 nF) devices, implying that Poly-TPD possesses the higher anti-disturbance capability than PEDOT:PSS, or lower conductance modulation under the bias voltage of 3 V (Fig. S11b). As for bilayer device, the widest frequency region and the largest variable quantity further unravel the strong enhancement of negative capacitance and conductance by the existence of interfacial dipoles (also in Supporting Note 2). Compared with single devices, the larger change in impedance (phase angle) of bilayer devices before and after applying voltage, in frequency range lower than 2×10^4 Hz, further reflects this tendency (Fig. S12). Hole interlayer not only gestates dipole interface and relieves the current amplification caused by energy level barrier, but also assimilates charge transport channels of Poly-TPD, against electrical perturbation. Dielectric systems will undergo repeated polarization under the action of an alternating electric field, resulting in losses [35–37]. Aiming in cross-checking the degree of polarization, the frequency- and bias-dependent quality factor (QF, reciprocal of dissipation factor), minutely indicate the degree of pure capacitance under voltage sweep (Fig. 3f). At 7×10^4 Hz, the single HTL devices all demonstrate the first QF extremum, three times larger than the second extremum (at 5×10^5 Hz) in PEDOT:PSS device. However, the first and second (at 3×10^5 Hz) extremum equals to each other in Poly-TPD device, coinciding with more ordered polarization in Poly-TPD featuring high localized states. In contrast, the maximum QF of bilayer device almost equals to that of PEDOT:PSS devices in the lower frequency domain (1×10^4 Hz). Furthermore, the matching of transition-frequency at which QF abruptly changes along with conductance is strong evidence for the fact that hole interlayer reconstructs energetic landscape of charge transport. Specifically, bilayer devices exhibit another extremum at 1×10^5 Hz, which is induced by the interfacial charge behavior between PEDOT:PSS and Poly-TPD. Even under the zero steady-state-potential, the slight alternative voltage disturbance would elicit obvious capacitive characteristics. And the inductive contribution to the capacitance is clearly resolved by plotting negative incremental curve of susceptance [38]. Among three devices, the hole-transit peak of PEDOT:PSS-only device locates at the lowest frequency (or longest τ), being consistent with the latest appeared space charge region in current-voltage curves [39]. And Poly-TPD-only device lies in the middle (Fig. S13a). Indeed, the hole interlayer with more disordered polarization direction and greater intensity builds plentiful carrier hopping channels between electrodes and HTL, ensuring the rapid and dynamic charge transfer, enhancing the proportion of capacitive characteristics and increasing the inductive effects. The higher phase angle of bilayer devices (72.9° at 146,500 Hz) than Poly-TPD devices (59.8° at 260, 700 Hz) further demonstrates the gradually prominent capacitive reactance behavior after the introduction of resistive hole interlayers with more delocalized states (Fig. S13b). Moreover, the clarification of hole interlayer-induced frequency-response differences provides a fresh insight for optimizing high-speed modulation capability of futuristic LED-based optical communication devices [40–42]. Specifically, the higher frequency-response (or higher modulation bandwidth) of a LED can be theoretically achieved by reducing the system capacitance and increasing the radiative recombination rate of emitting layer. And the charge transit time which injected carriers drift from terminals to recombination regions also plays a non-ignorable role in the optimization of high-speed LEDs [43]. The charge transit time of Poly-TPD-only device is greater than bilayer system, which seems to reduces its frequency-response capability when applied to optical communication. However, the introduction of hole interlayer enhances the capacitive proportion, especially at low frequencies. Alternating strong/weak ordered interfacial polarization helps to reduce capacitance, but increases charge transit time, whereas higher disorder and stronger interfacial polarization play the opposite role. The current of hole interlayer-free OLED under voltage pulse with various frequencies (Figure R14a-e) exhibits the more stable and pronounced switching response than that of the hole interlayer-included OLED (Figure R14f-j). Therefore, a compromise solution with both characteristics may be feasible. For example, a hole interlayer with higher mobility but lower capacitive characteristics could be employed. We emphasize that the frequency-dependent capacitance characteristics of each functional layer should be carefully considered when designing high speed LED-based (AC-driven or DC-driven) optical communication systems, including changes with the external electric field.

After dissecting the physics of interlayer-dependent hole-only devices, the resultant energetics are further investigated in OLEDs. Considering carrier injection-unbalanced characteristics of LEDs, a rising capacitance will occur owing to the accumulation of preferentially injected charges [44,45]. Although p-type Poly-TPD all directly contacts with n-type TPBi in two systems, charge imbalance in interlayer-dependent systems leads to the difference of field distribution. Considering the consistency of the preparation process, it is assumed that traps to the capacitance contribution in the same component remains unchanged despite the change of device architecture. Fig. 4a demonstrates that the phase angle in hole interlayer-included OLEDs gradually decreases with voltages increasing, especially at the lower frequencies. An obvious turning point occurs in the transition between 2.5 V and 3.0 V, which is consistent with the voltage when the EL spectrum is originally generated and efficient radiative recombination within Poly-TPD layer causes the step-down capacitance (Fig. S2d, Fig. S15a). That is, capacitive behaviors of the bilayer system begin to weaken when it reaches turn-on voltage, so does the impedance change (Fig. S15b). The response degree of the system capacitance and resistance with frequency under different driving voltages can be reflected by taking the first-order derivation of phase angle profiles (Fig. S16). With increasing voltages at higher frequencies, the phase angle increases more drastically. The higher voltage, the higher corresponding frequency at which the extreme value appears, ascribing to the weakening response of traps to electric field. However, when the frequency is less than 8×10^5 Hz, a trend of first falling then rising (3×10^5 Hz) and then falling (3×10^4 Hz) was exhibited at 2.5 V, while the first derivative value of the phase angle continues to decline at 3.0 V. This is consistent with the extremum of bilayer hole-only devices near 10^5 Hz, exhibiting charge transfer from PEDOT:PSS to Poly-TPD. Moreover, the resistive characteristics of the system dominate. As a comparison, the phase angle (or impedance) change with voltage is neither positively nor negatively correlated in OLEDs without hole interlayer. indicating the alternate domination of resistance and capacitance behaviors with voltage increasing. Nematic stripes with alternating strong and weak polarizations in Poly-TPD can verify this conclusion (Fig. 3A). Specifically, when electrodes directly contact Poly-TPD with ordered polarization direction and weaker intensity, the dynamic accumulation and dissipation of interfacial charges make the current slightly stagnate accompanied by increasing voltages (Figs. 1a, 1c). And this stagnation respites light-emitting generation of OLEDs without hole interlayer, leading to meager dependence of conductance (Fig. S17a) on voltages. Only when the voltage rises to a certain value could the influence of this ordered polarization can be overcome, and the carriers passing through Poly-TPD could be used for electroluminescence. While the conductance of OELDs equipped with hole interlayer featuring disordered polarization, demonstrates strong voltage dependence (Fig. S17b). With increasing voltages, interlayer-included OLEDs exhibit gradually decreasing capacitive reactance, and conversely, increasing capacitive reactance was attached to interlayer-free OLEDs, as shown in Fig. 4b. It means reactance characteristics of the system was reconstructed after introducing hole interlayer. Fig. 4c depicts the simplified models of hole-interlayer OLEDs, which are defined as PEPO (with interlayer) and PO (without interlayer), respectively. The system is approximately equivalent to a series-parallel connection of capacitors and resistors. According to the former reactance analysis, the vector diagram of OLEDs under operational voltage is plotted (Fig. 4d). Specifically, the hole interlayer conduces to the reduced capacitive reactance contribution and increased
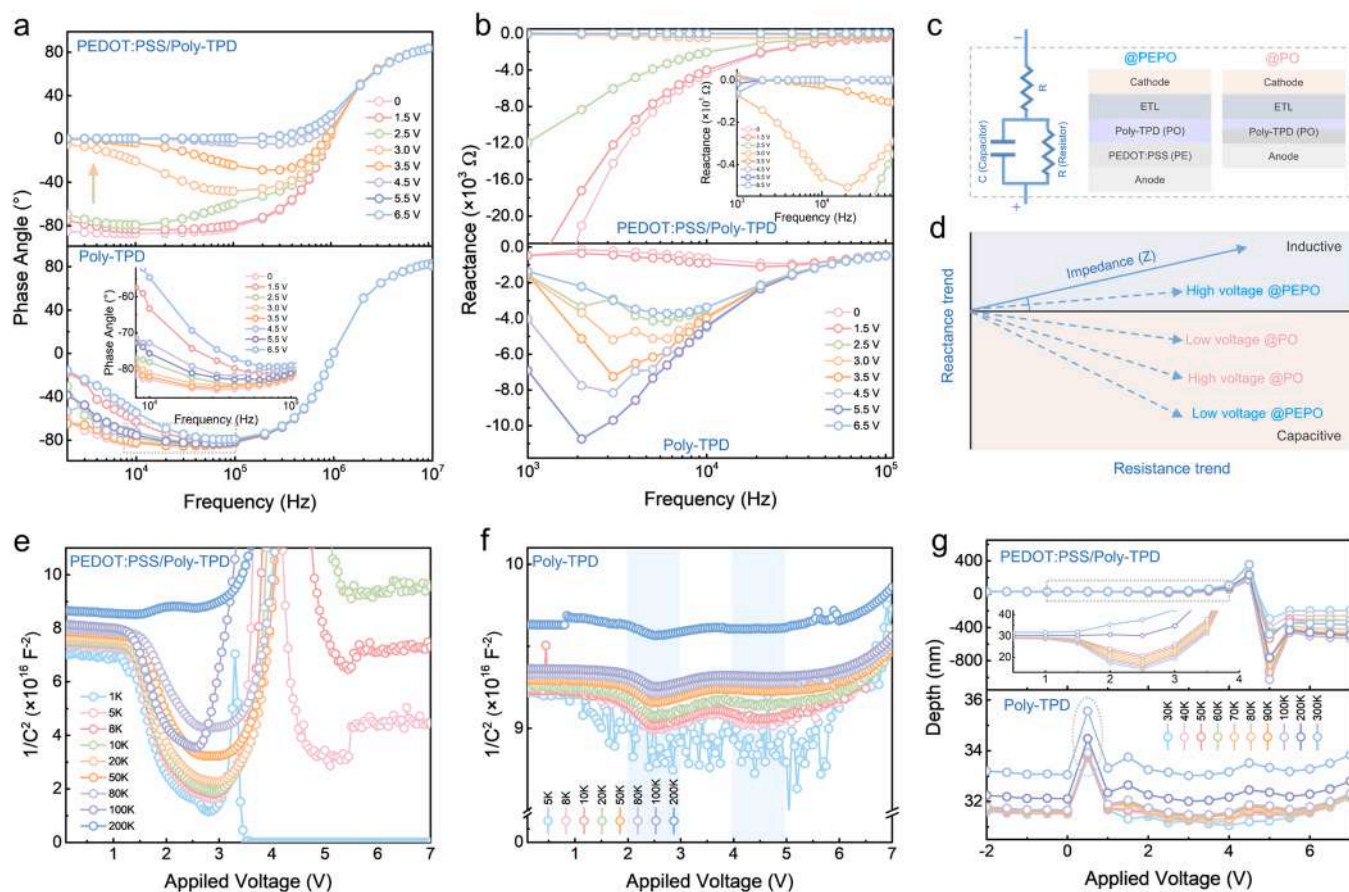
Fig. 4. Hole interlayer-dependent dynamical processes of OLEDs. (a) Phase angle and (b) reactance of PEDOT:PSS-included and PEDOT:PSS-free OLEDs. (c) Simplified models of PEDOT:PSS-dependent OLEDs. (d) Vector diagram for impedance of OLEDs under tests. Frequency-dependent inverse capacitance squared, $1/C^2$ of (e) PEDOT:PSS-included and (f) PEDOT:PSS-free OLEDs versus applied voltages. (g) Depletion depth as a function of voltage for OLEDs.

resistive proportion, of the OLEDs, when the voltage is lower than turn-on voltage (PEPO). And inductive effect occurs under normal electroluminescence of the devices. While PO is mainly characterized by capacitive reactance.

The electric field distribution was further probed by inverse capacitance squared ($1/C^2$) versus voltage according to Mott-Schottky (MS) [46–48]. In frequency domains lower than 80 K Hz, the $1/C^2$ of hole interlayer-contained OLEDs exhibits an apparently positive correlation with AC frequency (Fig. 4e). However, at a frequency of 100 K Hz, the $1/C^2$ curve experienced an abnormal drop at the voltage higher than 1.5 V, which can be attributed to the resonance of AC and carrier transport, the polarized electric field at PEDOT:PSS/Poly-TPD interface shields the AC disturbance [49,50]. The rising $1/C^2$ at 2.5 V corresponds to the failure of shielding and beginning of carrier recombination. As the applied voltages continue to rise, electroluminescence reaches saturation, $1/C^2$ begins to drop and tends to be constant, and the curve decreases faster at the lower frequencies. However, the $1/C^2$ curve of hole interlayer-free OLEDs does not decrease slightly until 2 V (Fig. 4f). Therefore, the higher electrical energy is required to compensate the interfacial potential energy loss which induced by the alternating strong/weak polarizations with Poly-TPD. This further proves the weaker electric field of ITO/Poly-TPD interface than PEDOT: PSS/Poly-TPD interface (Fig. 2d)[24,51,52]. Moreover, ascribing to the direct contact between electrodes and Poly-TPD with alternating strong-weak polarization, severe concussion characteristics appear in low frequency domain, which was also observed in hole-only Poly-TPD devices (Fig. S9b). Consistent with two jumps in J-V curves of perovskites LEDs and OLEDs without hole interlayer (Fig. 1a, c), the $1/C^2$ curve also exhibits two concave peaks (blue-gray areas in Fig. 4f). Only

after the second concave peak does the injected carriers begin to be actually used for the recombination of excitons to emit light, causing the capacitance to drop. The larger shift in Mott-Schottky behavior of PEDOT:PSS-free OLEDs originates from the regular polarization in Poly-TPD that induces a poorly replenished charge density and injection-limited contact between electrode and Poly-TPD. Fig. 4g precisely depicts the accumulation and recombination of interfacial carriers by measuring depletion depth versus applied voltages, and the depletion depth (W) is described as:

$$W = \frac{\varepsilon_s A}{C_p} \qquad (3)$$

where ε_s is the equivalent dielectric constant of device, A is the active area, C_p is the capacitance. Attributing to the increased capacitance by charge accumulation, the hole interlayer-included OLEDs experience a distinct downtrend of W at 1.5 V. After that, the occurrence of recombination reduces the charge accumulation, leading to a rising W (2.5 V), along with a sudden increase in dissipation factor (Fig. S18a). The efficient light emission under higher voltages makes the system capacitance sharply drop even become negative, consequently, a transition from the positive maximum (at 4.5 V) to the negative maximum depth (at 5.0 V) appears. And the higher frequency generates the larger W. In addition, the depletion depth of the PEDOT:PSS-included OLEDs is quite larger than the thickness of emission layers, which may be attributed to the sufficiently low ionizable impurities of PEDOT:PSS [52]. In marked contrast to that, a bulge begins to appear at 0 V when the hole interlayer is absent. Due to correlated disorder, especially the energetic disorder induced by orderly polarization and charge-dipole interactions at the interface, the charge injection from ITO to Poly-TPD is expected to be

spatially inhomogeneous [53]. The resultant dissipation restricts the exertion of interfacial capacitance behavior (Fig. S18b). Furthermore, a gently bulging peak (4–5 V) agrees with the second concave $1/C^2$ peak, indicating the initiation of carriers for recombination luminescence.

3. Conclusion

In summary, we have demonstrated, through imaged contact potential/polarization difference and multi-timed capacitance/voltage response, that alternant dominance of capacitance/resistance behaviors exists in which electrodes directly contacts light-emitting Poly-TPD with orderly alternating strong-weak polarization. This leads to the universally existing stagnation phenomenon of current density of LEDs with increasing voltages, only at the second increase can efficient EL be produced. The introduction of hole interlayer (PEDOT:PSS) exhibits more disordered polarization direction and greater intensity, leading to the generation of plentiful carrier hopping channels and enhanced electrical field. The rapid and dynamic charge transfer between ITO electrode and Poly-TPD ensures the J-V of LEDs with standard diode exponential change, which are conduced to the prominent capacitive reactance behaviors and resistive proportion at low voltages, and inductive reactance at high voltages. Also, we clarify this hole interlayer-dependent frequency-response difference for emerging high-speed modulation application. This work provides a fresh insight to unravel interfacial physics of LEDs for next-generation high-efficiency display and high-speed data-communication.

4. Experimental section

4.1. Materials

PEDOT:PSS (Clevios PVP AI4083), Poly (N,N′-bis(4-butylphenyl)-N, N′-bis(phenyl)-benzidine) (Poly-TPD, molecular weight, 20,000–60,000 g mol^{-1}), TPBi (98%) and LiF were purchased from Xi'an Polymer Light Technology Corp. CsPbBr$_3$ green quantum dots (in toluene, with a PL peak of 512 nm) were purchased from Najing technology Co., Ltd. Chlorobenzene (extra dry, 99.9%) and ethanol (extra dry, 99.5%) were purchased from Aladdin Reagents. All chemicals were directly used as received, unless otherwise stated.

4.2. Device fabrication

The patterned ITO glasses were firstly scrubbed with a glasses cloth soaked in optical detergent, and then consecutively cleaned with deionized water, acetone, isopropanol and ethanol under sonication for 15 min each, and then dried with compressed N$_2$. treated with UV-ozone for 30 min before spin-coating. For hole interlayer-included devices, PEDOT:PSS was spin-coated on the ITO substrates at 5000 r.p.m. for 50 s and healed at 120 °C for 30 min in air. When cooled to room temperature, the all samples were transferred into a N$_2$-filled glovebox (H$_2$O <0.01 ppm, O$_2$ < 0.01 ppm) subsequent processes. Poly-TPD solutions (in chlorobenzene, 8 mg mL^{-1}) were spin-coated at 3500 r.p.m. for 40 s and baked at 110 °C for 30 min. For perovskite QDs-included LEDs, CsPbBr$_3$ QDs (in toluene, 20 mg mL^{-1}) was then spin-coated onto the Poly-TPD layer at 2000 r.p.m. for 1 min. Last, TPBi (30 nm), LiF (1 nm), Al electrode (70 nm) were deposited using a thermal evaporation system under a high vacuum (less than 10^{-4} Pa). Film deposition parameters were the same as those for the fabrication of organic LEDs (without perovskite QDs).

4.3. Characterization

The current density-voltage-luminance (J-V-L) characteristics and electroluminescence spectrum of LEDs were measured using a Keithley 2400 source meter combined with a spectrometer (QE-Pro, Ocean Optics) and an integration sphere (FOIS-1, Ocean Optics). The surface

potential, height distribution, phase and amplitude were operated by a MultiMode8 atomic force microscope (Bruker Corporation) under frequency-modulation (FM) KPFM model, and the conductive tips, coated with PtIr, were used. The resonance frequency and the spring constant are 75 kHz and 3.0 N m^{-1}, respectively. The capacitance-voltage-frequency (C-V-F), conductance, depth and quality factor measurement were conducted using multi-frequency CV model of keithley 4200 parameter analyzer. Electrochemical impedance spectroscopy (frequency range from 0.1 Hz to 100,000 Hz) was measured with CHI660E electrochemical workstation. The high-speed current response was performed on Fs-Pro semiconductor parameter testing system.

CRediT authorship contribution statement

Cheng Yan: Conceptualization, Methodology, Investigation, Formal analysis, Writing-original draft, Visualization. **Xiankan Zeng**: Investigation. **Qungui Wang**: Investigation. **Xiaodong Peng**: Investigation. **Wen Li**: Formal analysis. **Jingjing Cao**: Formal analysis. **Yue Gao**: Formal analysis. **Xiang Chu**: Formal analysis. **Xuehai Fu**: Formal analysis. **Shiyu yang**: Formal analysis. **Yongjian Chen**: Formal analysis. **Weiqing Yang**: Writing-review & editing, Funding acquisition, Supervision.

Declaration of Competing Interest

The authors declare that they have no known competing financial interests or personal relationships that could have appeared to influence the work reported in this paper.

Data availability

Data will be made available on request.

Appendix A. Supporting information

Supplementary data associated with this article can be found in the online version at doi:10.1016/j.nanoen.2022.107621.

References

[1] H. Cho, S.-H. Jeong, M.-H. Park, Y.-H. Kim, C. Wolf, C.-L. Lee, J.H. Heo, A. Sadhanala, N. Myoung, S. Yoo, S.H. Im, R.H. Friend, T.-W. Lee, Science 350 (2015) 1222–1225.

[2] T.-H. Han, Y. Lee, M.-R. Choi, S.-H. Woo, S.-H. Bae, B.H. Hong, J.-H. Ahn, T.-W. Lee, Nat. Photonics 6 (2012) 105–110.

[3] P.K.H. Ho, J.-S. Kim, J.H. Burroughes, H. Becker, S.F.Y. Li, T.M. Brown, F. Cacialli, R.H. Friend, Nature 404 (2000) 481–484.

[4] N.B. Kotadiya, H. Lu, A. Mondal, Y. Ie, D. Andrienko, P.W.M. Blom, G.A. H. Wetzelaer, Nat. Mater. 17 (2018) 329–334.

[5] O. Bubnova, Z.U. Khan, H. Wang, S. Braun, D.R. Evans, M. Fabretto, P. Hojati-Talemi, D. Dagnelund, J.B. Arlin, Y.H. Geerts, S. Desbief, D.W. Breiby, J. W. Andreasen, R. Lazzaroni, W.M. Chen, I. Zozoulenko, M. Fahlman, P.J. Murphy, M. Berggren, X. Crispin, Nat. Mater. 13 (2014) 190–194.

[6] A.W. Grice, D.D.C. Bradley, M.T. Bernius, M. Inbasekaran, W.W. Wu, E.P. Woo, Appl. Phys. Lett. 73 (1998) 629–631.

[7] R.L.Z. Hoye, M.L. Lai, M. Anaya, Y. Tong, K. Galkowski, T. Doherty, W. Li, T. N. Huq, S. Mackowski, L. Polavarapu, J. Feldmann, J.L. MacManus-Driscoll, R. H. Friend, A.S. Urban, S.D. Stranks, ACS Energy Lett. 4 (2019) 1181–1188.

[8] B.B. Zhang, S. Yuan, J.P. Ma, Y. Zhou, J. Hou, X. Chen, W. Zheng, H. Shen, X. C. Wang, B. Sun, O.M. Bakr, L.S. Liao, H.T. Sun, J. Am. Chem. Soc. 141 (2019) 15423–15432.

[9] M. Liu, Q. Wan, H. Wang, F. Carulli, X. Sun, W. Zheng, L. Kong, Q. Zhang, C. Zhang, Q. Zhang, S. Brovelli, L. Li, Nat. Photonics 15 (2021) 379–385.

[10] G. Li, Z.K. Tan, D. Di, M.L. Lai, L. Jiang, J.H. Lim, R.H. Friend, N.C. Greenham, Nano Lett. 15 (2015) 2640–2644.
[11] F. Meng, X. Liu, X. Cai, Z. Gong, B. Li, W. Xie, M. Li, D. Chen, H.L. Yip, S.J. Su, Nanoscale 11 (2019) 1295–1303.
[12] F. Yan, J. Xing, G. Xing, L. Quan, S.T. Tan, J. Zhao, R. Su, L. Zhang, S. Chen, Y. Zhao, A. Huan, E.H. Sargent, Q. Xiong, H.V. Demir, Nano Lett. 18 (2018) 3157–3164.
[13] Z. Chen, Z. Li, C. Zhang, X.F. Jiang, D. Chen, Q. Xue, M. Liu, S. Su, H.L. Yip, Y. Cao, Adv. Mater. 30 (2018), e1801370.
[14] Z. Fang, W. Chen, Y. Shi, J. Zhao, S. Chu, J. Zhang, Z. Xiao, Adv. Funct. Mater. 30 (2020), 1909754.
[15] S. Chu, W. Chen, Z. Fang, X. Xiao, Y. Liu, J. Chen, J. Huang, Z. Xiao, Nat. Commun. 12 (2021) 147.
[16] C. Giebeler, H. Antoniadis, D.D.C. Bradley, Y. Shirota, J. Appl. Phys. 85 (1999) 608–615.
[17] H. Antoniadis, J.N. Miller, D.B. Roitman, I.H. Cambell, IEEE Trans. Electron Devices 44 (1997) 1289–1294.
[18] Q.J. Sun, B.H. Fan, Z.A. Tan, C.H. Yang, Y.F. Li, Y. Yang, Appl. Phys. Lett. 88 (2006), 163510.
[19] Y. Yin, Z. Deng, Z. Lü, X. Li, M. Li, B. Liu, Y. Wang, F. Teng, Displays 38 (2015) 32–37.
[20] X. Liang, S. Bai, X. Wang, X. Dai, F. Gao, B. Sun, Z. Ning, Z. Ye, Y. Jin, Chem. Soc. Rev. 46 (2017) 1730–1759.
[21] M. Fahlman, S. Fabiano, V. Gueskine, D. Simon, M. Berggren, X. Crispin, Nat. Rev. Mater. 4 (2019), 627-624.
[22] Z. Chen, Z. Li, T.R. Hopper, A.A. Bakulin, H.L. Yip, Rep. Prog. Phys. 84 (2021), 046401.
[23] R.T. White, E.S. Thibau, Z.H. Lu, Sci. Rep. 6 (2016) 21109.
[24] M. Zhang, Q. Chen, R. Xue, Y. Zhan, C. Wang, J. Lai, J. Yang, H. Lin, J. Yao, Y. Li, L. Chen, Y. Li, Nat. Commun. 10 (2019) 4593.
[25] Z. He, C. Zhong, X. Huang, W.Y. Wong, H. Wu, L. Chen, S. Su, Y. Cao, Adv. Mater. 23 (2011) 4636–4643.
[26] F. Ebadi, N. Taghavinia, R. Mohammadpour, A. Hagfeldt, W. Tress, Nat. Commun. 10 (2019) 1574.
[27] W.P. Gomes, D. Vanmaekelbergh, Electrochim. Acta 41 (1996), 967-963.
[28] J.R. Macdonald, W.B. Johnson, Fundamentals of impedance spectroscopy, Impedance Spectroscopy (2018) 1–20.
[29] M. Bag, L.A. Renna, R.Y. Adhikari, S. Karak, F. Liu, P.M. Lahti, T.P. Russell, M. T. Tuominen, D. Venkataraman, J. Am. Chem. Soc. 137 (2015) 13130–13137.
[30] J. Jamnik, J. Maier, J. Electrochem. Soc. 146 (1999) 4183–4188.
[31] P.L. Taberna, P. Simon, J.F. Fauvarque, J. Electrochem. Soc. 150 (2003) 292–300.
[32] D. Wang, K.H. Chan, N.K. Elumalai, M.A. Mahmud, M.B. Upama, A. Uddin, S. Pillai, Phys. Chem. Chem. Phys. 19 (2017) 25016–25024.
[33] H. Sirringhaus, P.J. Brown, R.H. Friend, M.M. Nielsen, K. Bechgaard, B.M. W. Langeveld-Voss, A.J.H. Spiering, R.A.J. Janssen, E.W. Meijer, P. Herwig, D. M. de Leeuw, Nature 401 (1999) 685–688.
[34] A. Abutaha, P. Kumar, E. Yildirim, W. Shi, S.W. Yang, G. Wu, K. Hippalgaonkar, Nat. Commun. 11 (2020) 1737.
[35] T.P. Nguyen, V.H. Tran, Mater. Sci. Eng. B 31 (1995) 255–260.
[36] W. Kauzmann, Rev. Mod. Phys. 14 (1942) 12–44.
[37] A.K. Jonscher, J. Phys. D: Appl. Phys. 32 (1999) R57–R70.
[38] H.C.F. Martens, J.N. Huiberts, P.W.M. Blom, Appl. Phys. Lett. 77 (2000) 1852–1854.
[39] H.C.F. Martens, H.B. Brom, Phys. Rev. B 60 (1999) 8489–8492.
[40] A. Ren, H. Wang, W. Zhang, J. Wu, Z. Wang, R.V. Penty, I.H. White, Nat. Electron. 4 (2021) 559–572.
[41] C. Bao, W. Xu, J. Yang, S. Bai, P. Teng, Y. Yang, J. Wang, N. Zhao, W. Zhang, W. Huang, F. Gao, Nat. Electron. 3 (2020) 156–164.
[42] W. Deng, X. Jin, Y. Lv, X. Zhang, X. Zhang, J. Jie, Adv. Funct. Mater. (2019), 1903861.
[43] K. Yoshida, P.P. Manousiadis, R. Bian, Z. Chen, C. Murawski, M.C. Gather, H. Haas, G.A. Turnbull, I.D.W. Samuel, Nat. Commun. 11 (2020) 1171.
[44] D.Y. Kondakov, J.R. Sandifer, C.W. Tang, R.H. Young, J. Appl. Phys. 93 (2003) 1108–1119.
[45] S. Chen, W. Cao, T. Liu, S.W. Tsang, Y. Yang, X. Yan, L. Qian, Nat. Commun. 10 (2019) 765.
[46] O. Almora, C. Aranda, E. Mas-Marzá, G. Garcia-Belmonte, Appl. Phys. Lett. 109 (2016), 173903.
[47] J.A. Carr, S. Chaudhary, Energy Environ. Sci. 6 (2013).
[48] C. Yan, C. Luo, W. Li, X. Peng, J. Cao, X. Zeng, Y. Gao, X. Fu, X. Chu, W. Deng, F. Chun, S. Yang, Q. Wang, W. Yang, ACS Appl. Mater. Interfaces 13 (2021) 57560–57566.
[49] G. Blatter, F. Greuter, Phys. Rev. B Condens Matter 33 (1986) 3952–3966.
[50] R.A. Awni, Z. Song, C. Chen, C. Li, C. Wang, M.A. Razooqi, L. Chen, X. Wang, R. J. Ellingson, J.V. Li, Y. Yan, Joule 4 (2020) 644–657.
[51] P. Juhasz, J. Nevrela, M. Micjan, M. Novota, J. Uhrik, L. Stuchlikova, J. Jakabovic, L. Harmatha, M. Weis, Beilstein J. Nanotechnol. 7 (2016) 47–52.
[52] J.C. Scott, J. Vac. Sci. Technol. A. 21 (2003) 521–531.
[53] S.V. Novikov, G.G. Malliaras, Phys. Rev. B 73 (2006), 033308.